Controllable growth on Nano-graphite-supported ZrO_2-MnO_x bimetallic oxides for electrocatalytic antibiotics degradation: Boosting mechanism of Mn^{3+}/Mn^{4+} redox cycle

Si Duan [a], Guihong Lan [a, *], Xiaoting Yang [b], Yongqiang Liu [c], Haiyan Qiu [a], Bo Xu [a], Yuan Gao [a], Zhuang Xie [a]

a Southwest Petr Univ, Sch Chem & Chem Engn, Chengdu 610500, Sichuan, PR China.

b Eternal Chemical (Chengdu) Co., Ltd., Qionglai 611534, Sichuan, China.

c Faculty of Engineering and Physical Sciences, University of Southampton, Southampton SO17 1 BJ, UK.

* Corresponding author at: Southwest Petr Univ, Sch Chem & Chem Engn, Chengdu 610500, Sichuan, PR China.

E-mail addresses: guihonglan416@sina.com (Guihong Lan).

Abstract

Antibiotic contamination has become one of the most pressing problems in the field of water purification. Using Nano-graphite (Nano-G) as carbon carrier, ZrO_2-MnO_x/Nano-G composite electrode with high catalytic activity was prepared by hot pressing method based on MnO_x/Nano-G prepared by sol-gel method. The results show that the ZrO_2-MnO_x/Nano-G electrode reduces charge transfer resistance while improving surface oxygen desorption ability. MnO_x can catalyze the two-electron reduction of O_2 to produce H_2O_2, which can then be converted to ·OH and $\cdot O_2^-$. Thereafter, the results of free radical capture experiments confirmed that $\cdot O_2^-$ played a significant role in the electrocatalytic degradation of tetracycline hydrochloride (TC) by a ZrO_2-MnO_x/Nano-G composite electrode. Furthermore, the abundant hydroxyl group on the surface of Nano-G and ZrO_2 particles can be used as an active site for catalyzing the Mn^{3+}/Mn^{4+} redox reaction, resulting in the generation of more free radicals. The high efficiency electrocatalytic degradation of TC was achieved through the synergistic action of the three. Under optimal reaction conditions, the degradation rate of TC reached 93% after 120 min of electrolysis. ZrO_2-MnO_x/Nano-G displayed good stability following 10 cycles of degradation experiments. Finally, the potential TC degradation pathway was investigated using liquid chromatography-mass spectrometry (LC-MS) and density functional theory (DFT), and the degradation mechanism was clarified.

Keywords

Tetracycline hydrochloride; ZrO_2-MnO_x/Nano-G; Electrocatalytic oxidation

1. Introduction

Antibiotics are frequently used due to their capacity to inhibit and destroy bacteria and pathogenic microorganisms. However, since antibiotics cannot be absorbed by organisms, their incomplete

metabolized active agents are continuously discharged into the water and persist there, where they have turned into a typical environmental pollution[1,2]. Tetracycline hydrochloride (TC), one of them, is the second most widely used antibiotic in the world, as a broad-spectrum antibiotic with numerous applications in the fields of medicine[3], aquaculture and animal husbandry[4]. Furthermore, depending on the environmental conditions, the TC can damage ecosystems by causing antibiotic resistance, drug-resistant microorganisms and harmful impacts on living things, as well as harming human health through the food chain[5,6]. Thus, Novel composite materials and preparation methods are therefore urgently needed to effectively eliminate antibiotic contaminants from the water environment.

Membrane separation[7], adsorption[8,9], advanced oxidation processes (AOPs)[10] and biological method[11] are well established and extensively used in industrial water pollutant removal. AOPs are one of the representative and proven processes, which include Fenton method[12], ozone oxidation[13], photocatalytic oxidation[14] and electrochemical oxidation[15]. However, conventional wastewater treatment processes have disadvantages in removing antibiotics, and electrochemical advanced oxidation processes (EAOPs) as the only treatment technology that does not add any reagent to the wastewater[16]. Typically, EAOPs use electrons to attack oxides or water to generate the corresponding free radicals, thus achieving the removal of pollutants. It is not only superior to other chemical wastewater treatment methods, but also simpler to operate and has a higher degradation efficiency for antibiotics and other refractory organic matter.

Generally speaking, the positive electrode materials used for EAOPs are mainly concentrated on carbon materials with good electrical conductivity and chemical stability, such as carbon felt[17], graphite[18], boron doped diamond (BDD)[19] and metal–organic frameworks (MOFs)[20]. However,

although traditional porous materials such as MOF and mesoporous silica[21] have large specific surface area and high porosity, they are not suitable as electrochemical catalysts due to poor electrical conductivity. So far, some studies have made up for its poor electrical conductivity by carbonizing modification strategies[22,23]. Nano-graphite (Nano-G) has high porosity and ultra-fine particles[24]. It has the general characteristics of conventional carbon materials plus a bigger specific surface area and good electrical conductivity[25]. Consequently, the Nano-G electrode has the potential to achieve high efficiency in the electrochemical oxidation of antibiotics. Studies have shown that the electrochemical degradation efficiency of antibiotics can be further enhanced by the uniform loading of catalyst materials on the surface of the Nano-G electrode[26]. Recently, metal oxides have recently been introduced into the field of electrochemistry as electrocatalytic active materials due to their environmental friendliness, non-toxicity, high stability, and good catalytic activity. Tang et al.[27] obtained a 46.7% improvement in degradation efficiency by modifying MoO_3 on the surface of Nano-G and Li et al.[28] reported that the composite anode RuO_2-TiO_2/Nano-G exhibited benefits in the production of ·OH, the synergistic effects between RuO_2, TiO_2 and Nano-G, which enhance specific surface area, increase electrochemical oxidation activity and reduce charge transfer resistance. According to research, the introduction of oxygen defects in metal oxides can not only improve the conductivity and band structure of the materials, but also effectively regulate the local electronic environment around the catalytic site and improve the electrocatalytic activity[29].

Transition metals have a variety of valence states because of the insufficient valence shells, which make it easier for electrons to escape[30,31]. Of which, Mn in manganese oxides (MnO_x) can form active structural defects by converting oxidation states, resulting in a high surface oxygen desorption

capacity and sufficient surface oxygen vacancies, which can greatly enhance electron transfer on the surface of MnO_x[32]. As a result, MnO_x exhibits superior catalytic activity in the EAOPs. At the same time, the combination of MnO_x and Nano-G not only makes up for its poor conductivity defect, but is also considered an effective catalyst for oxygen reduction and ·OH formation[33]. In addition, zirconium dioxide (ZrO_2) possesses advantageous electrochemical and physical characteristics, including low toxicity, high stability, biocompatibility, and excellent electron transport and surface charge qualities[34]. The abundant hydroxyl group on the surface of Nano-G and ZrO_2 particles can be employed as the active site to catalyze the redox reaction of Mn^{3+}/Mn^{4+}.

In this work, ZrO_2-MnO_x/Nano-G composite catalyst was prepared by progressive controlled growth, where the flake overlay was successfully realization using hot pressing and sol-gel methods with Nano-G as the support mesh. In conjunction with the results of the cyclic voltammetry (CV) and electrochemical impedance spectroscopy (EIS) analyses, the charge transfer resistance (R_{ct}) reduced and the oxygen evolution potential (OEP) increased. This was attributable to the synergistic action of ZrO_2, MnO_x and Nano-G to increase the reaction site and electrochemical oxidation activity. On the one hand, the ZrO_2-MnO_x/Nano-G composite electrode boosts the conductive network's mass transfer rate and catalytic performance. On the other hand, the desorption ability of the Nano-G electrode's surface oxygen is improved, resulting in a wider range of surface oxygen vacancies, increasing active sites and promoting TC degradation. On TC degradation efficiency, the effects of catalyst dose, current density, plate distances, pH value and initial TC concentration were evaluated. The kinetics of TC degradation, as well as potential degradation mechanisms and pathways were explored. Eventually, the degradation pathway of TC was analyzed by LC-MS and density functional theory (DFT) to further elucidate the mechanism.

2. Experimental

2.1 Reagents

Tetracycline hydrochloride ($C_{22}H_{24}N_2O_8 \cdot HCl$) was provided by Shanghai Aladdin Biochemical Technology Co., Ltd. Nano-graphite was obtained from Qianhai Jishengya (Shenzhen) Technology Co., Ltd. Potassium permanganate ($KMnO_4$), zirconium nitrate ($Zr(NO_3)_4 \cdot 5H_2O$) , polyethylene glycol 400 (PEG400), ammonia solution ($NH_3 \cdot H_2O$), sodium sulfate anhydrous (Na_2SO_4) , sodium hydroxide (NaOH) , absolute ethanol (C_2H_5OH), sulfuric acid and nitric acid were purchased from Chengdu Kelon Co., Ltd. and were all analytically pure. Manganese (II) acetate ($(CH_3COO)_2Mn$) was provided by Tianjin Damao Chemical Reagent Factory. Poly tetra fluoroethylene (PTFE) was obtained from Dajin Fluorine Chemical (China) Co., Ltd. All solutions, unless otherwise noted, were prepared using ultrapure water with a resistivity of > 18 mΩ cm at room temperature.

2.2 Preparation of electrodes

The specific synthesis process is depicted in Scheme 1. MnO_x/Nano-G composites were made using the sol-gel method. Typically, manganese acetate (0.1593 g) was dissolved in deionized water, followed by the addition of polyethylene glycol (PEG) 400 and Nano-G, all of which were added while stirring. After mixing, add potassium permanganate solution (0.1 mol L^{-1}, 6.4 mL) and heat to 80 °C for 30 min, filtered to remove the precipitate, and then washed repeatedly with deionized water and absolute ethanol. After drying at 80 °C, MnO_x/Nano-G was obtained by calcination at 400 °C in muffle furnace for 2 h. What's more, ZrO_2 nanoparticles were synthesized by sol-gel and coprecipitation methods[35].

ZrO_2-MnO_x/Nano-G cathode was prepared as previous research[36]. 3.0 g of MnO_x/Nano-G were dispersed in absolute ethanol and sonicated for 2 h. 0.75 mL of PTFE (60 wt%) and ZrO_2 powder

were added in turn and mixed, and kept under sonication for 30 min to form a sticky shape. Hot pressing the resulting mixture onto a titanium web (as a base) and drying it results in electrodes.

On a CS310H electrochemical workstation (Wuhan Kesite Instruments Co., Ltd., China) outfitted with a three-electrode system, all of the electrochemical analyses were carried out. ZrO_2-MnO_x/Nano-G composite electrode, Pt electrode and saturated calomel electrode (SCE) were used as working electrode, opposite electrode and reference electrode, respectively. The power supply was a programmable linear power supply (SS-L303SPL).

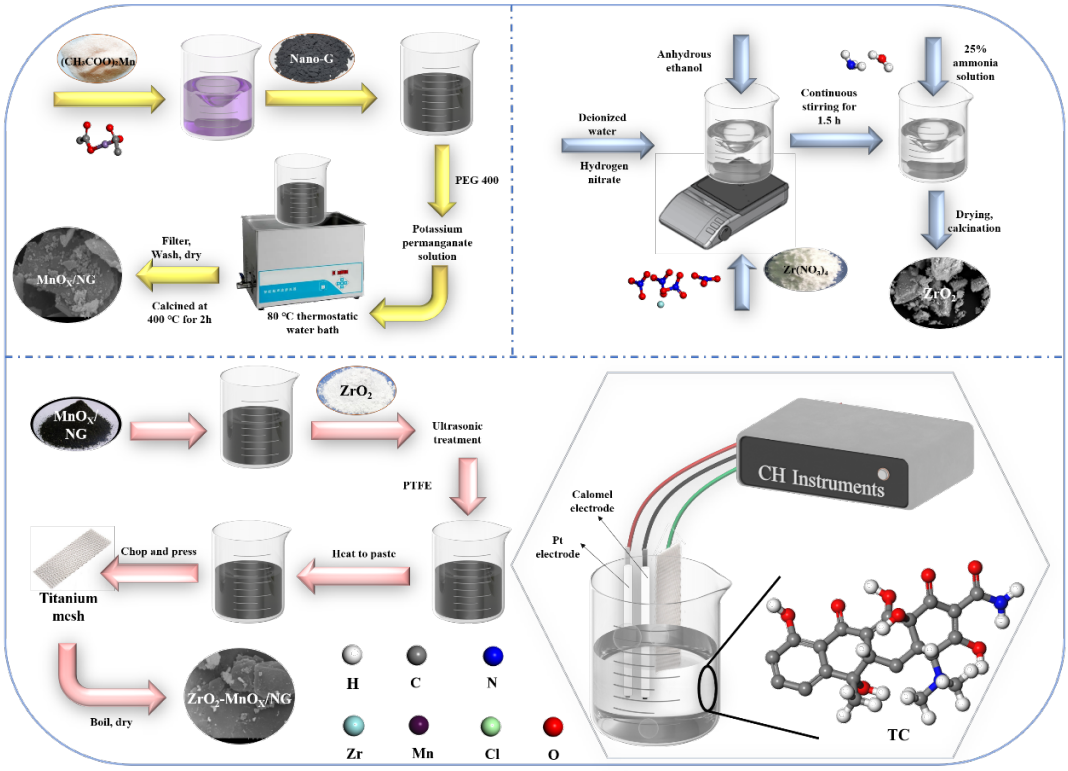

Scheme 1. Processes of construction of ZrO_2-MnO_x/Nano-G cathode.

2.3 Characterizations

The internal structure and surface morphology of the samples were characterized by field emission transmission electron microscopy (TEM, FEI Tecnai G2 F20) and scanning electron microscopy (SEM, SU3500). A Bruker AXS D8 Advance X-ray diffractometer was used to analyze the crystalline structures using X-ray diffraction (XRD). The elements and chemical states on the

sample's surface were analyzed using an X-ray photoelectron spectrometer (XPS). The test condition is that the X-ray source was Mono AlKa, the energy was 1486.6 eV, the voltage was 15 kV, the beam was 15 mA, and the analyzer's scanning mode was CAE. A Brunauer-Emmett-Teller (BET) analyzer was used to investigate the surface area and pore size (ASAP2460). N_2 adsorbed gas was used as the test gas, and the test conditions included a temperature of -195.850 °C, a 6 s equilibrium interval, a sample density of 1.000 g cm^{-3}, and no low-pressure dose. The surface elements were characterized by energy dispersive X-ray spectroscopy (EDS, SU3500). The Raman spectrometer (IM-52) was used to characterize the chemical structure of samples in the range of 2000 - 200 cm^{-1}. The fixed laser wavelength was 785 nm and the resolution was 4 cm^{-1}.

2.4 Electrocatalytic degradation process

The electrochemical oxidation was carried out in a glass reactor (5 cm × 6 cm × 5 cm) equipped with constant temperature magnetic stirrer. Iridium Ruthenium electrode (RuO_2-IrO_2/Ti) as anode, ZrO_2-MnO_x/Nano-G electrode cathode (effective area of each plate is 20 cm^2) were placed in parallel. As an electrolyte, 0.1 mol L^{-1} Na_2SO_4 was used, and TC was chosen as a pollutant model. The factors that influence the degradation process were evaluated.

2.5 Analytical methods

Throughout the experiment, samples were taken periodically and the absorbance at the maximum absorption wavelength (276.4 nm) after filtration in a 0.45 μL microporous membrane was determined using an UV-visible spectrophotometer (UV-1800, Shimadzu Enterprise Management Co., Ltd., China). A first-order kinetic model was used to fit the degradation data, and the rates of degradation under each scenario were examined.

$$\ln (C_0/C_t) = kt \quad (1)$$

Where C_0 (mg L^{-1}) means the starting TC concentration, C_t (mg L^{-1}) is the TC concentration in the solution electrocatalytically degraded within time t, and k stands for the pseudo-first-order rate constant.

A flame atomic absorption spectrophotometer was used to determine whether manganese ion leaching occurred during the electrochemical degradation of TC. Both the biological oxygen demand (BOD_5) and chemical oxygen demand (COD_{Cr}) were calculated. On a Hypersil GOLD column (100 mm × 2.1 mm, 1.9 μm), the primary intermediates were examined using LC-MS.

3. Results and discussion

3.1 characterization

The surface morphology of the prepared sample was observed by SEM. Obviously, Nano-G in Fig. 1a and b shows a laminated structure with a fairly smooth surface[37]. After loading MnO_x, the surface is densely arranged with irregular nanoparticles. In Fig. 1c, ZrO_2 particles have irregular shape and relatively rough surface. As shown in Fig. 1d, the large specific surface area of Nano-G provides a platform for the good growth of MnO_x and ZrO_2. There are some uneven grooves and gaps on the surface of MnO_x/Nano-G and ZrO_2-MnO_x/Nano-G composite electrodes, as illustrated in Fig. 1e and f. The layered structure of Nano-G, on the other hand, was not discernible, indicating that the electrode was well prepared. The electrode not only features a rich channel structure to increase the specific surface area, but it can also establish an excellent conductive network to promote H_2O_2 generation in the cathode. Additionally, Fig. S1 studies the element distribution of the Nano-G, ZrO_2, MnO_x/Nano-G and ZrO_2-MnO_x/Nano-G composites. It can be shown that the composites contain C, O, Mn and Zr when combined with the change of element percentage content in Table S1. Furthermore, the EDS elemental mapping illustrated that the elementals C, O, Zr and Mn were uniformly distributed in ZrO_2-MnO_x/Nano-G composites (Fig. 1g), confirming the successful doping of ZrO_2 in the synthesis process.

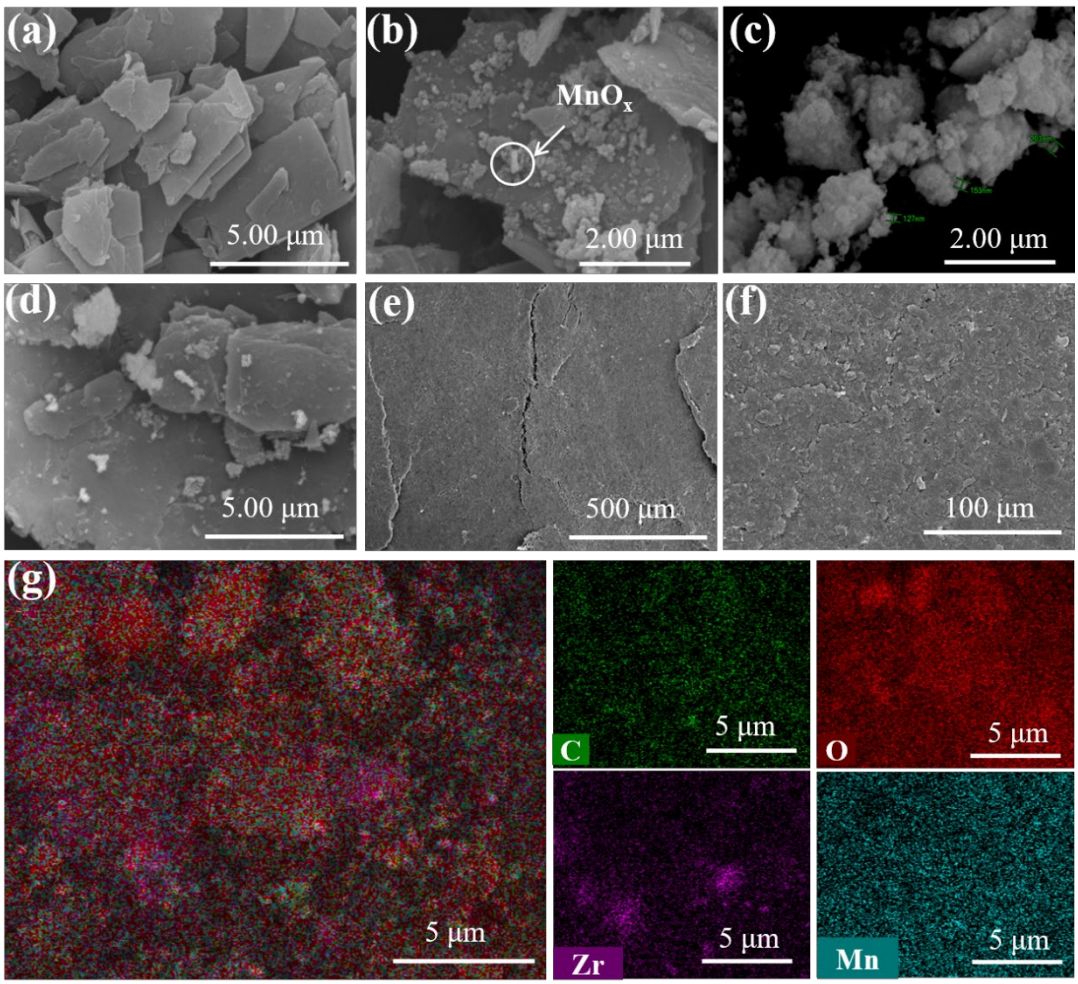

Fig. 1 SEM images of (a) Nano-G, (b) MnO_x/Nano-G composite material, (c-d) ZrO_2 and ZrO_2-MnO_x/Nano-G composite material, (e-f) MnO_x/Nano-G and ZrO_2-MnO_x/Nano-G composite electrode; (g) SEM-EDS elemental mapping images of ZrO_2-MnO_x/Nano-G composite material.

Then, the structure of MnO_x/Nano-G composite was confirmed by TEM. As shown in Fig. 2a, Nano-G and MnO_x nanoparticles can be clearly observed, and MnO_x nanoparticles are undoubtedly anchored to the Nano-G sheet structure. More importantly, high-resolution transmission electron microscopy (HRTEM) of MnO_x shows that the lattice fringe with interplanar spacing of approximately 0.23 nm and 0.48 nm, which are assigned to the (222) plane of Mn_2O_3 and the (101) plane of MnO_2, respectively, which confirms the existence of multiple valence states of manganese in MnO_x/Nano-G. Particularly, the interaction of MnO_x and Nano-G results in good electrical conductivity, which is conducive to improving electrochemical performance. Fig. 2d shows the EDS element mapping results, which verify the successful preparation of MnO_x/Nano-G composites.

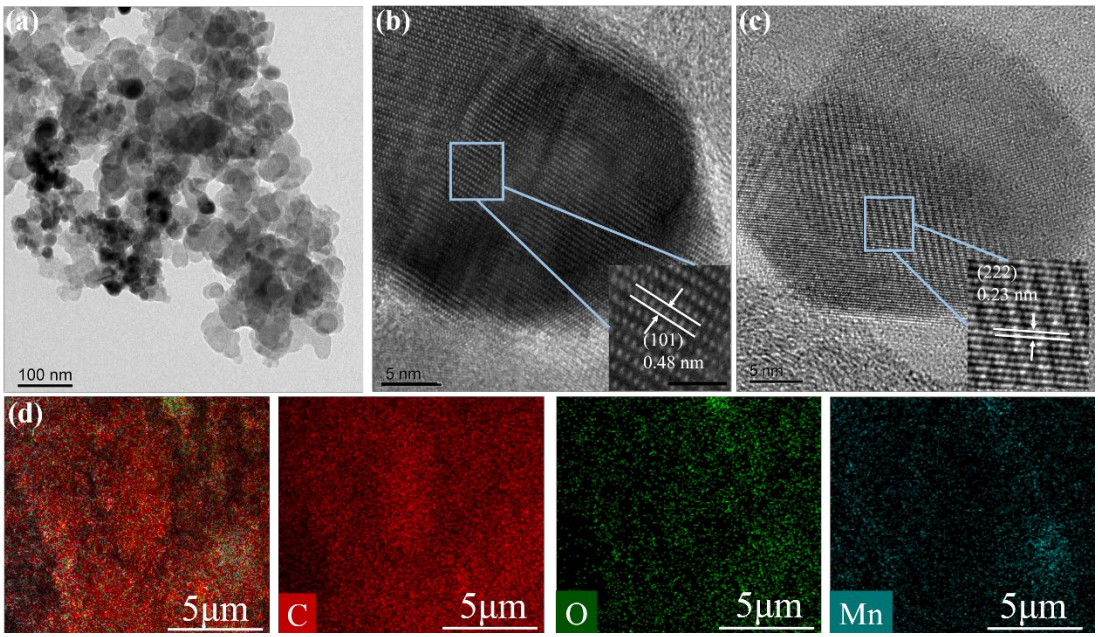

Fig. 2 (a) TEM images of MnO_x/Nano-G; (b-c) HRTEM image of MnO_x; (d) SEM-EDS elemental mapping images of MnO_x/Nano-G composite material.

The crystal structure of the material was characterized by XRD pattern. ZrO_2 exhibits distinctive diffraction peaks at 2θ = 28.40°, 31.66°, 54.36°, 58.24° and 62.16° as shown in Fig. 3a. The diffraction peaks of Nano-G at about 26.8° and 54.9° are consistent with previous report[38]. Particularly, there are some peaks at around 45° for Nano-G, which is usually caused by the layer spacing. It can be inferred that the layer spacing of Nano-G is small, and there is a highly stacked ordered graphite layer structure. For MnO_x/Nano-G composites, the distinctive diffraction peaks of MnO_2 and Mn_2O_3 emerge at 36.3°, 42.6°, 57.6° and 43.3°. Fig. 3b clearly shows the efficacy of ZrO_2 doping.

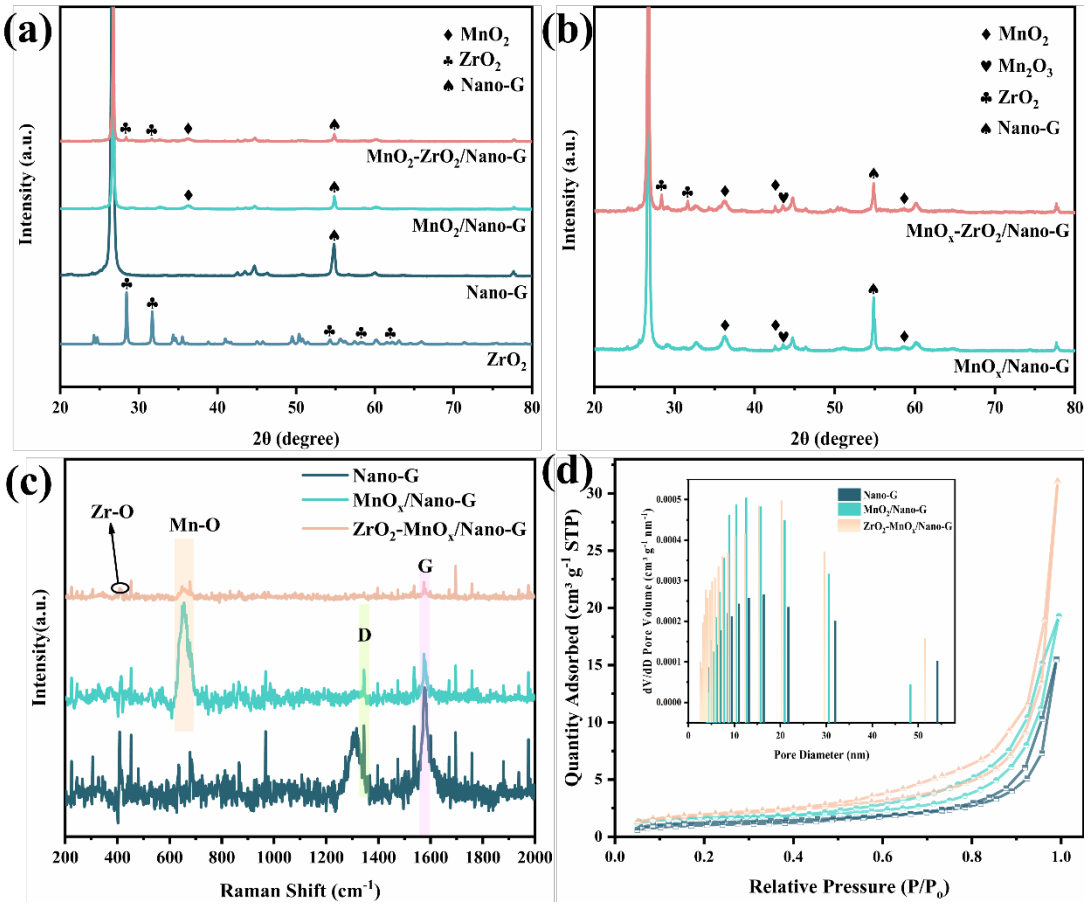

Fig. 3 (a) XRD of ZrO_2, Nano-G, MnO_2/Nano-G composite and ZrO_2-MnO_2/Nano-G composite; (b) XRD of MnO_x/Nano-G composites and ZrO_2-MnO_x/Nano-G composites; (c) Raman spectra of Nano-G, MnO_x/Nano-G and ZrO_2-MnO_x/Nano-G composites; (d) N_2 adsorption-desorption isotherms and pore-size distribution (Inset) curves of Nano-G, MnO_2/Nano-G composite and ZrO_2-MnO_x/Nano-G composite.

The Raman spectra of Nano-G, MnO_x/Nano-G and ZrO_2-MnO_x/Nano-G composites are shown in Fig. 3c. The Mn-O vibration is responsible for the peak at 648.02 cm^{-1}. Besides, the vibration peaks at 343.84 and 410.53 cm^{-1} correspond to Zr-O. The other two apparent peaks at 1344.74 and 1574.27 cm^{-1} could be attributed to graphite's usual D and G bands, respectively. The D band represents C atom lattice defects, while the G band represents the in-plane stretching vibration of C atom sp^2 hybridization[39]. The N_2 adsorption-desorption isotherms and pore-size distribution of Nano-G,

MnO_2/Nano-G and ZrO_2-MnO_2/Nano-G composite electrodes, as shown in Fig. 3d, are typical type IV isotherms with H_3 hysteresis loops. It is a typical mesoporous material with uneven pore size distribution. ZrO_2-MnO_x/Nano-G has the maximum specific surface area and pore volume. In conclusion, more active sites are present in the ZrO_2-MnO_x/Nano-G composite electrode, which is favourable for the electrocatalytic degradation of TC[40].

XPS was used to record the chemical state and elemental composition of ZrO_2-MnO_x/Nano-G, as shown in Fig. 4a. Peaks of O 1s, Mn (2p and 3s), Zr 3d and C 1s indicated the presence of O, Mn, Zr and C in the sample. Gaussian-Lorentzian curve fitting was used to analyse the high-resolution XPS spectra of Mn 2p, Zr 3d and O 1s (Fig. 4b, c and d). The spectrum of Mn $2p_{3/2}$ shows three peaks, one for Mn_2O_3 (641.82 eV) and two for MnO_2 (640.32 and 644.33 eV). The results confirm that MnO_x in the synthesized ZrO_2-MnO_x/Nano-G catalyst is in a mixed valence state, which makes the reduction/oxidation reaction between Mn^{3+} and Mn^{4+} possible[41]. Meanwhile, In the fine spectrum of Zr (Fig. 4c), the binding energies of 181.58eV and 183.91eV can be attributed to the characteristic peaks of Zr 3d5/2 and Zr 3d3/2, indicating the presence of Zr^{4+}[42,43], which are lower than the values of ZrO_2 reported in the literature[44]. As illustrated in Fig. 4d, the deconvolution of O 1s peaks corresponded to six components originating from the Mn-O (around 529.06 eV), Zr-O (around 529.36 eV), and at 530.45 eV there is physically-adsorbed O[45], O-C-O (around 531.67 eV), -C=O (around 532.71 eV)[46], and -C-O- (around 533.61 eV)[47]. Therefore, XPS analysis further demonstrated the successful preparation of the ZrO_2-MnO_x/Nano-G composite electrode.

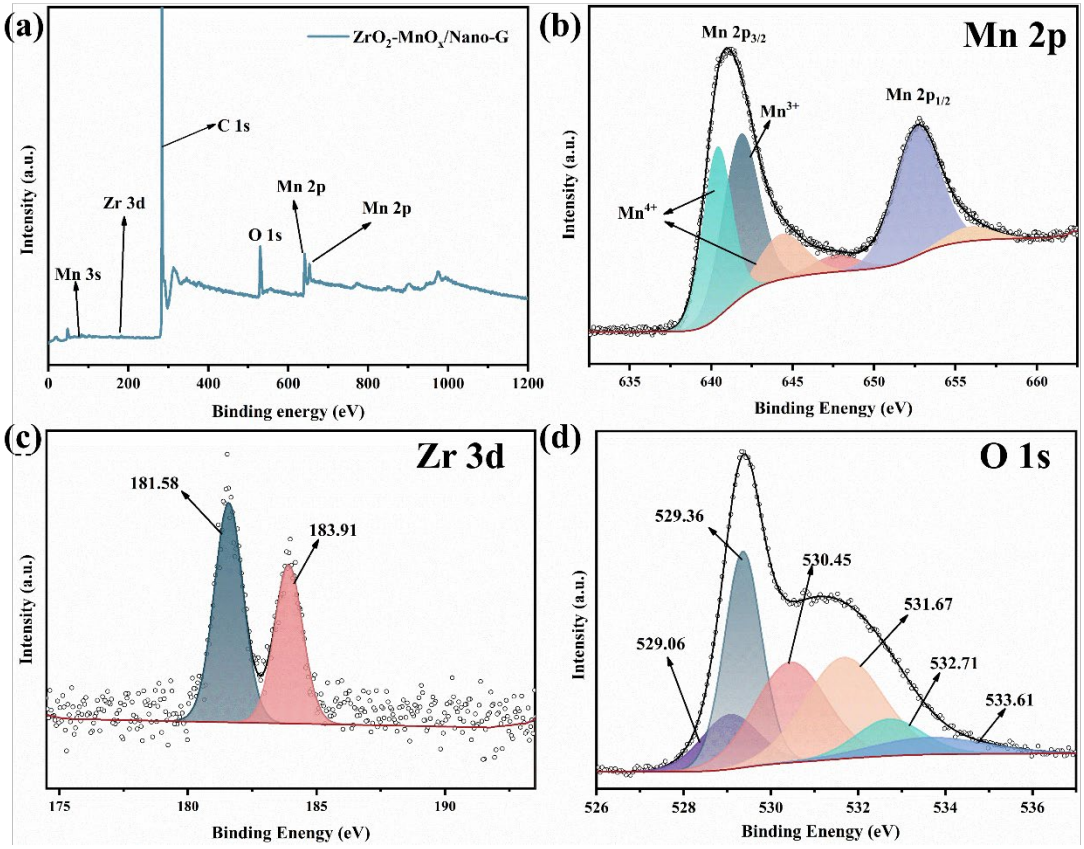

Fig. 4 XPS survey spectra of the (a) ZrO_2-MnO_x/Nano-G; the high-resolution XPS spectra of (b) Mn 2p and (c) Zr 3d, (d) O 1s.

3.2 Electrochemical performance test of electrodes

The electrocatalytic performance of the composite or its surface materials loaded on the electrodes was evaluated using EIS. In the high frequency range, the half-arc diameter corresponds to the charge transfer resistance (Rct), and in the low frequency range, the intercept of the slash line and the real axis of the impedance corresponds to the overall solution's uncompensated resistance (Ru). Comparing the semi-arc radii of the two composite electrodes in Fig. 5a, the ZrO_2-MnO_x/Nano-G electrode has a smaller semi-arc radius. The equivalent circuit in the figure was used for data fitting, and the Rct of ZrO_2-MnO_x/Nano-G composite electrode is calculated to be 551500 Ω, which is less than that of MnO_x/Nano-G composite electrode (2398000 Ω). Observing the low frequency range, the Ru of ZrO_2-MnO_x/Nano-G is the smallest, which means the solution resistance has the least

influence on the entire system. These outcomes imply that the addition of MnO_x and ZrO_2 decreases the barrier of electron transfer at the interface, resulting in lower diffusion resistance and higher electrochemical capacitance[48].

Fig. 5b shows the CV curves of three different electrodes in 0.1 M Na_2SO_4. The peak current density of ZrO_2-MnO_x/Nano-G composite electrode (4.96×10^{-6} A/cm^2) is greater than that of MnO_x/Nano-G composite electrode (4.06×10^{-6} A/cm^2) and Nano-G electrode (1.66×10^{-6} A/cm^2). Furthermore, the oxidation peak current density of the ZrO_2-MnO_x/Nano-G composite electrode is around 0.55V. The peak potential is positive when compared to MnO_x/Nano-G composite electrode, indicating that doping ZrO_2 can make MnO_x/Nano-G composite electrode has higher OEP. High OEP allows for the production of more ·OH and $\cdot O_2^-$, which accelerate the breakdown of pollutant molecules and improve the ability of organic matter to degrade. Furthermore, higher OEP tends to create more active sites and a greater variety of surface oxygen vacancies[49]. To summarise, the doping of MnO_x and ZrO_2 enhances the electrochemical performance of the modified electrode and increases TC degradation ability.

The increase of electrochemically active site is one of the main reasons for the improvement of catalytic performance, so it is necessary to calculate the value of electrochemically active surface area (ECSA). Typically, the CV curves of the electrodes at various scanning rates are drawn first, followed by the current density curve plotted in terms of the scanning rate. The electrochemically active surface area (ECSA) is calculated based on the slope of this curve, which is equal to the double-layer capacitance (C_{dl}). The CV results of the electrodes are displayed in Fig. S2a-c. In the meantime, Fig. S2d displayed the outcomes of the C_{dl} value that were computed based on each electrode's scanning speed curve and current density difference. The results show that the C_{dl} value

of MnO_x/Nano-G is higher than that of single Nano-G catalyst, and the C_{dl} value of ZrO_2-MnO_x/Nano-G is the largest, indicating that transition metal oxide doping is an effective means to improve the catalytic activity. We calculated ECSA to further support this finding and found that ZrO_2-MnO_x/Nano-G (1.07 cm^2) > MnO_x/Nano-G (0.93 cm^2) > Nano-G (0.47 cm^2). With the increase of the electrochemical active area, the available sites of the electrochemical reaction increase, thus improving the electrocatalytic activity.

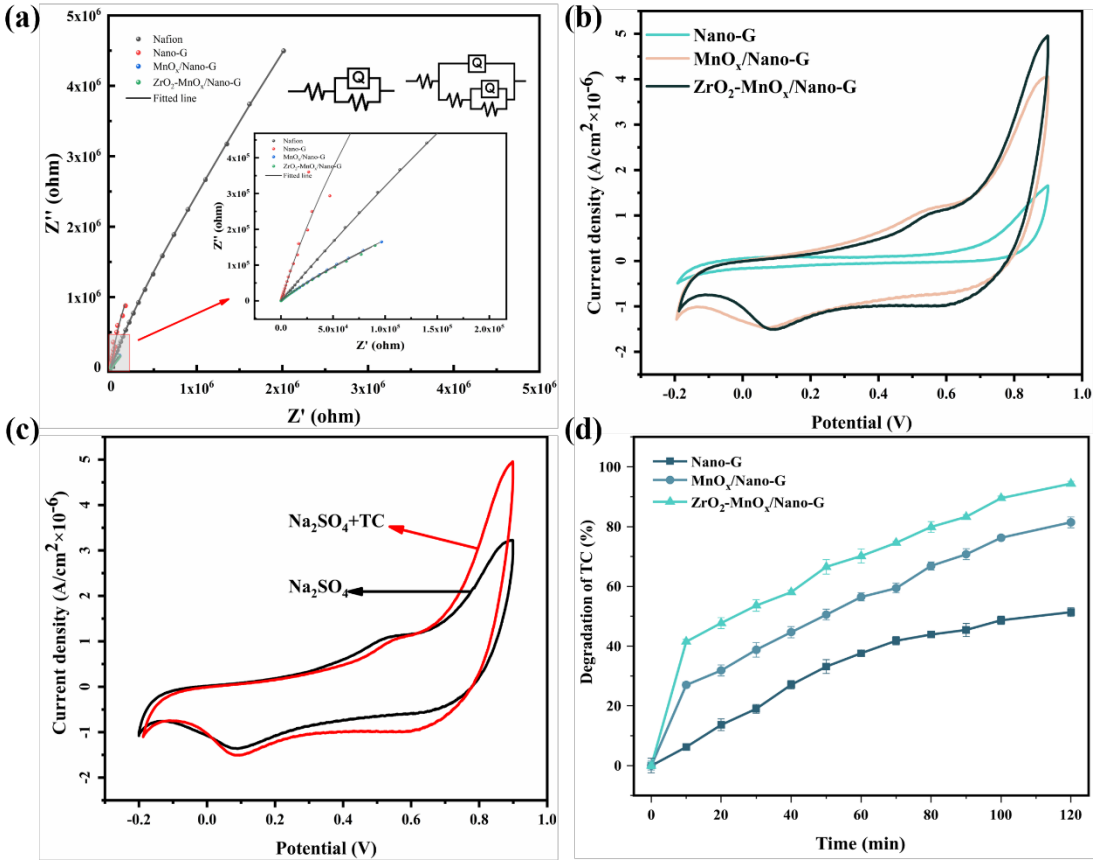

Fig. 5 (a) EIS of Nafion, Nano-G, MnO_x/Nano-G and ZrO_2-MnO_x/Nano-G electrodes, inset shows the magnified view in high-frequency region, the frequency range was 100 kHz to 0.01 Hz; (b) CV curves of the Nano-G, MnO_x/Nano-G and ZrO_2-MnO_x/Nano-G electrodes at a scan rate of 2 mV s^{-1}; (c) CV curve of ZrO_2-MnO_x/Nano-G without TC (black) and with 20 mg L^{-1} TC (red); (d) Effect of different cathodes on degradation of TC. Both of the tests were conducted in 0.1 mol L^{-1} Na_2SO_4 solution.

To investigate the possible oxidation pathway of TC, CV scans were recorded using ZrO_2-MnO_x/Nano-G electrodes in the absence and presence of 20 mg L^{-1} TC. No oxidation peak was observed when TC was added to the electrolyte, as shown in Fig. 5c, demonstrating that TC did not have direct electron transfer on the cathode surface. In other words, TC was oxidized and decomposed in the solution via indirect electrochemical oxidation and oxidants (such as free radicals).

To degrade TC, nano-G, MnO_x/Nano-G, and ZrO_2-MnO_x/Nano-G electrodes were used as cathodes, and electrolysis was performed for 120 min under the identical experimental conditions. The signal in Fig. 5d shows that the degradation efficiency of the ZrO_2-MnO_x/Nano-G electrode is significantly higher than that of the MnO_x/Nano-G electrode and Nano-G electrode. This result suggests that the ZrO_2-MnO_x/Nano-G electrode speeds up electron transport and two-electron reduction of O_2. Furthermore, it catalyzes the production of free radicals and affects the TC degradation in the solution.

The performance of the electrochemical oxidation is significantly influenced by the experimental conditions. Here, the efficiency of TC electrocatalytic degradation by ZrO_2-MnO_x/Nano-G was systematically assessed. The degradation process followed pseudo-first-order kinetics under all conditions. The effects of current density, initial concentration, plate distance and solution pH on TC degradation by ZrO_2-MnO_x/Nano-G electrode and its kinetics were analyzed.

First of all, according to Fig. 6a, the degradation rate of TC increases first and then decreases as the initial concentration increases. Within 120 min, the TC degradation rate reached 94.55% when the TC concentration was 20 mg L^{-1}. But at 35 mg L^{-1}, the removal rate is reduced. This is due to the limited amount of $\cdot OH$, $\cdot O_2^-$ and H_2O_2 oxidants produced on the cathode at higher concentrations,

which influences the degradation rate of TC. Furthermore, more intermediates may be produced, competing with the antibiotic for the active site, resulting in more antibiotics remaining unreacted. The *k* value change in Fig. 6b and c is consistent with the degradation rate, demonstrating that at higher initial concentrations, the antibiotic and the intermediate compete for ·OH radicals[50]. As a result, the degradation effect is best when the initial TC concentration is 20 mg L^{-1}.

Because the rate of ·OH formation is dependent on the applied current density, the current density is regarded as a crucial operating parameter in the electrocatalytic degradation process. According to Fig. 6d, as the applied current density increased, the degradation rate of TC first increased and then decreased. This is mainly due to the fact that an increase in current density will speed up electron transfer on the cathode plate and produce more H_2O_2, which will cause more ·OH and $\cdot O_2^-$ to react with TC[51]. However, if the current density is too high, the battery voltage in the electrochemical degradation will rise. During this time, side reactions like hydrogen evolution and oxygen reduction to water at the cathode will take place, which will impede the TC's ability to degrade. Besides, an excessive amount of applied current may deactivate the adhesive, releasing the active component from the electrode and ultimately slowing down the degradation rate of TC. A pseudo-first-order kinetic model of TC degradation at various current densities was fitted (Fig. 6e). The corresponding *k* value is shown in Fig. 6f. In the following experiments, the current density of 30 mA cm^{-2} is used because *k* is maximum at this current density.

The effect of different plate distances on the electrocatalytic degradation of TC is analyzed in Fig. 6g. The TC degradation efficiency at 5 mm, 10 mm and 15 mm is 76.96%, 96.25% and 71.62%, respectively. As a result, the degradation efficiency of TC is highest when the electrode plate distance is 10 mm. This is because a larger plate distance will result in greater resistance between

the electrodes and a smaller effective current density. As a result, TC was unable to be transferred to the vicinity of the cathode in time, and intermediate products were unable to be transferred to the solution in time. The contact between the electrode and the TC is reduced, which slows the rate of degradation. What's more, excessive distance can result in energy loss. On the contrary, when the distance is too small, even though the effective current density is increased, the electrode life is shortened, resulting in temperature rise and even short circuit phenomenon. The degradation of TC at various electrode distances was fit using a pseudo-first-order kinetic model, as shown in Fig. 6h. The *k* of TC degradation at various electrode distances is depicted in Fig. 6i. *k* reaches its maximum (23.02 $min^{-1}\times10^{-3}$) at a distance of 10 mm. In summary, the ideal plate distance for TC electrochemical degradation is 10 mm.

By adjusting pH values from 3 to 11 with diluted NaOH and H_2SO_4 solutions, the effect of initial pH value on electrochemical oxidation of TC was explored (Fig. 6j). A pseudo-first-order kinetic model was used to fit the degradation process of TC at different pH values, and the results are shown in Fig. 6k and l. It has been discovered that the degradation rate and *k* of TC can reach the maximum value (96.33 %, 15.89 $min^{-1}\times10^{-3}$) when the initial pH value is 5.0. In other circumstances, the rate of TC degradation showed a downward trend, becoming even slower when the pH level was higher than 5.0 or even just slightly alkaline. It is clear that the degradation of TC in environments that are too acidic or too basic is poor. Lower pH values are advantageous for increasing the overpotential of O_2 and decreasing side reaction of oxygen evolution[52]. Thus, this will lead to the production of more ·OH radicals, which is advantageous for mineralization.

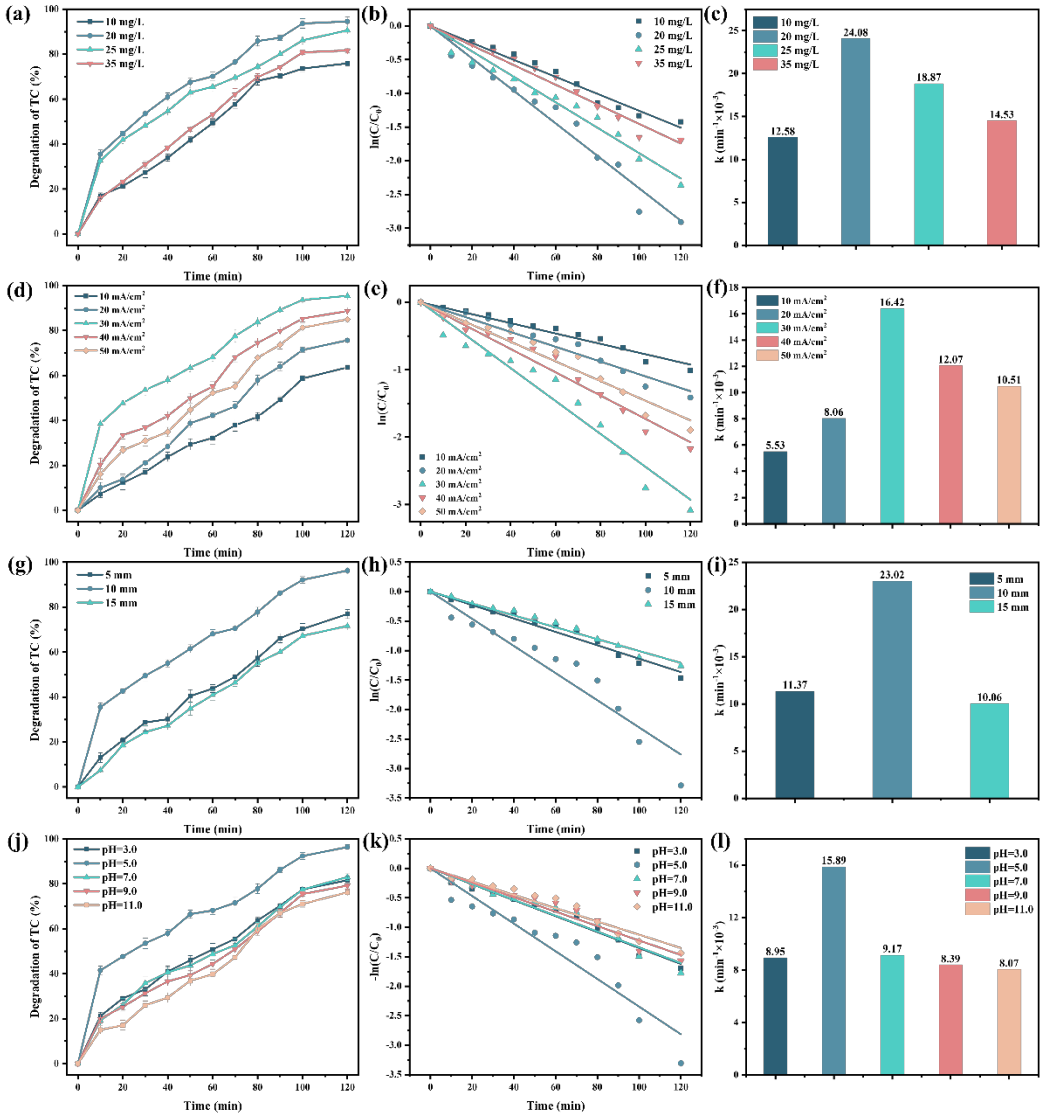

Fig. 6 Performance of ZrO_2-MnO_x/Nano-G electrode for TC degradation: (a) initial concentration, (d) current density, (g) plate distances, (j) solution pH, (b, e, h, k) the corresponding first-order kinetics and (c, f, i, l) rate constant.

3.3 Performance of ZrO_2-MnO_x/Nano-G cathode for treating antibiotic wastewater

To assess the reusability and stability of the ZrO_2-MnO_x/Nano-G electrode. Electrocatalytic degradation experiments were carried out for ten cycles under optimal electrolytic conditions. Fig. 7a shows that after three cycles, the degradation efficiencies were 96.24%, 91.07% and 90.46%, respectively. The degradation effect of TC tended to be stable after 10 cycles, confirming the

desirable reusability of ZrO_2-MnO_x/Nano-G electrode. In order to check whether manganese ion leaching occurs during the electrocatalytic degradation of TC by using ZrO_2-MnO_x/Nano-G electrode. The content of manganese ion in the solution was determined regularly by flame atomic absorption spectrophotometer (SP-3520AA). Fig. 7b shows that no manganese ion was detected during the first 30 min. After that, the concentration of manganese ion gradually rose until it peaked at 0.15 mg L^{-1} at 120 min and then remained stable. It can be explained that as the reaction progresses, the electrode is exposed to a strong oxidizing environment and applied current for a long period of time. This causes the electrode's adhesive to gradually deactivate, thus leaching manganese ions from the electrode into the solution. Despite the manganese ion leaching in the ZrO_2-MnO_x/Nano-G composite electrode, its concentration is below the permitted limit of 2 mg L^{-1} in the Discharge standards of pollutants for municipal wastewater treatment plants (GB 18918-2002). As a result, the leaching concentration of manganese ion is within the allowable emission range and can be purified by the environment's self-purification capacity.

Fig. 7c depicts the pH change during degradation. It can be seen that the pH of the solution decreases with the electrolytic reaction in the process of TC degradation. Within 10 min, it starts to decline quickly, and between 10 and 120 min later, it starts to slow down. It's possible that a portion of TC is breaking down, producing intermediates with carboxyl groups and causing a sharp pH drop. Then, because of the oxidation of free radicals and other active substances produced during the electrolysis process, the pH slowly decreases. It is worth noting that the pH slightly rises at the start, which, as shown by Eq. (2) and (3), is due to the hydrogen evolution reaction producing a large amount of OH^-. Furthermore, inorganic ions in antibiotic wastewater, such as chloride ions, sulfate ions and phosphate ions, may be converted to acidic compounds, causing pH changes.

$$O_2+H_2O+2e^-\rightarrow HO_2\cdot+OH^- \quad (2)$$

$$HO_2\cdot+H_2O\rightarrow H_2O_2+OH^- \quad (3)$$

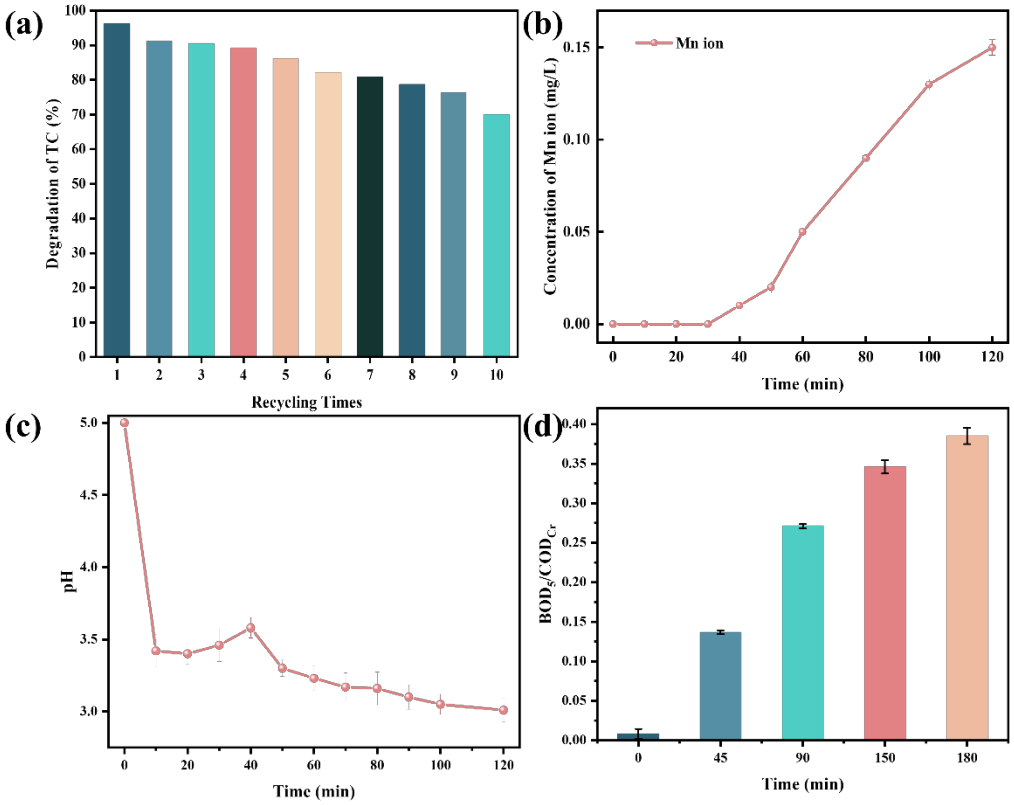

Fig. 7 (a) Effect of cycle times of ZrO_2-MnO_x/Nano-G composite electrode on degradation of TC; (b) The concentration of manganese ions in solution as a function of reaction time; (c) Change of solution pH during degradation of TC; (d) BOD_5/COD_{Cr} of TC at different electrolytic times.

Fig. 7d show BOD_5/COD_{Cr} (B/C) at different electrolytic times to evaluate the biodegradability of TC after electrochemical degradation. The B/C values of TC gradually increased as the electrolysis time was extended, reaching 0.385 at 120 min. At this time, TC wastewater has good biodegradability, which can meet the requirements of subsequent biochemical system treatment. Because of the radical attack during the degradation process, group substitution and ring opening reactions will occur, determining the resistance, biotoxicity and other chemical properties of TC. Therefore, the chemical properties of TC changed after electrochemical degradation[53]. The

biodegradability of TC can be gradually improved by using a ZrO_2-MnO_x/Nano-G composite electrode as the cathode.

3.4 Intermediates identification and proposed TC degradation pathway

To identify the types of free radicals present in the solution and the indirect electrochemical oxidation. After 120 min of degradation, the concentration of TC solution without scavenger, TC solution with isopropyl alcohol (IPA), and TC solution with p-benzoquinone (P-BQ) were measured (Fig. S3). The results show that after adding the two scavengers, the degradation rate of TC decreases, indicating that $\cdot O_2^-$ and ·OH exist in the electrochemical degradation process of TC. When P-BQ ($\cdot O_2^-$-trap) was added, the degradation rate of TC decreased to 51.23%, while IPA (·OH -Trap) decreased to 66.91%. In other words, the addition of two types of scavengers inhibited TC degradation. P-BQ was added, which resulted in a slower rate of degradation, suggesting that $\cdot O_2^-$ contributed more to TC degradation. As a result, it is easy to conclude that $\cdot O_2^-$ is the most active substance in improving the degradation rate of TC, followed by ·OH. These indications suggest that electrocatalytic degradation of TC is an indirect process.

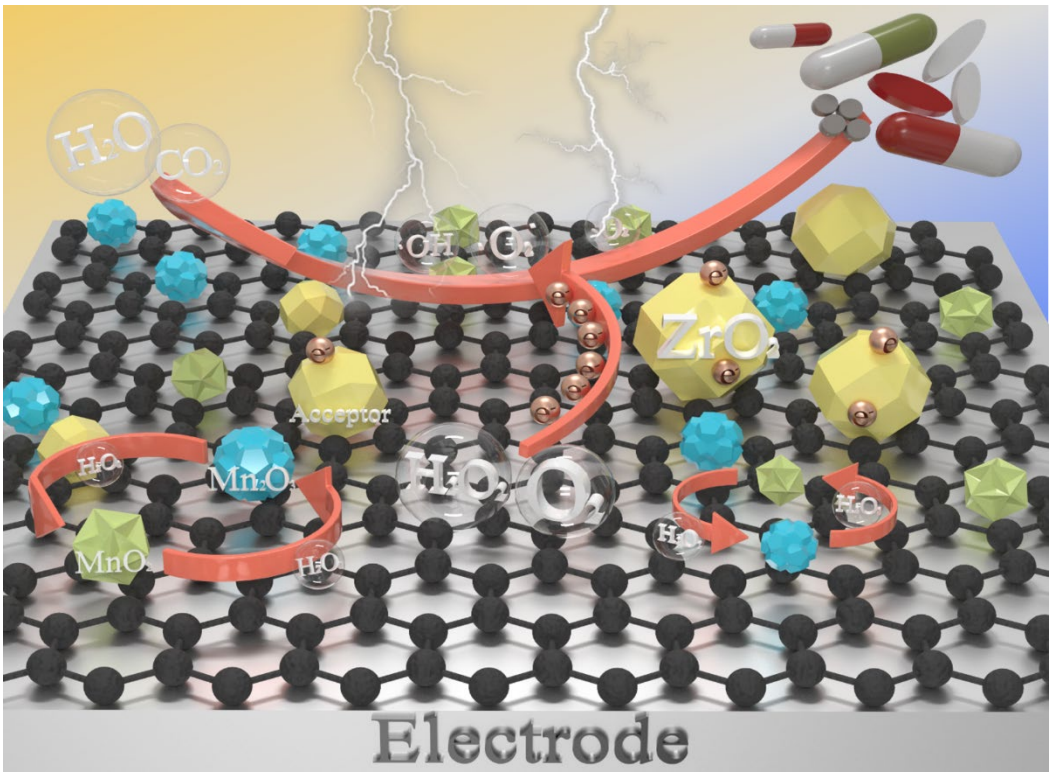

Scheme 2. The mechanism of electrochemical oxidation degradation of TC.

Based on the aforementioned findings, the electrochemical oxidation degradation mechanism of TC was proposed. According to Eq. (4)-(9), hydrogen peroxide (H_2O_2) can be formed in situ by two-electron reduction of O_2 in the ZrO_2-MnO_x/Nano-G composite electrode. At the same time, H_2O_2 can be converted to ·OH and $·O_2^-$ radicals due to the excellent catalytic activity of MnO_x. The applied current causes a large number of electrons to be produced by the ZrO_2-MnO_x/Nano-G composite electrode. In addition, ZrO_2 offers a greater specific surface area, more active sites and good surface charge performance, all of which can significantly lower the charge transfer resistance of ZrO_2-MnO_x/Nano-G electrodes. Consequently, ZrO_2 functions as an accepter to trap more electrons to the electrode. On the one hand, electrons in the solution combine with dissolved oxygen and water to produce large amounts of ·OH and $·O_2^-$, which participate in the degradation of TC. On the other hand, more electrons can indirectly facilitate the conversion between Mn^{4+} and Mn^{3+}, increasing the generation of ·OH and $·O_2^-$. Eventually, because of the strong oxidation capacity of

H_2O_2, ·OH and $\cdot O_2^-$, organic matter is mineralized to CO_2 and H_2O.

$$O_2 + 2H_2O + 2e^- \rightarrow H_2O_2 + 2OH^- \quad (4)$$

$$Mn(IV) + H_2O_2 \rightarrow H^+ + HO_2\cdot + Mn(III) \quad (5)$$

$$Mn(III) + H_2O_2 \rightarrow OH^- + \cdot OH + Mn(IV) \quad (6)$$

$$H_2O_2 + HO_2\cdot + e^- \rightarrow \cdot OH + \cdot O_2^- + H_2O \quad (7)$$

$$\cdot OH + organic \rightarrow \ldots \rightarrow CO_2 + H_2O \quad (8)$$

$$\cdot O_2^- + organic \rightarrow \ldots \rightarrow CO_2 + H_2O \quad (9)$$

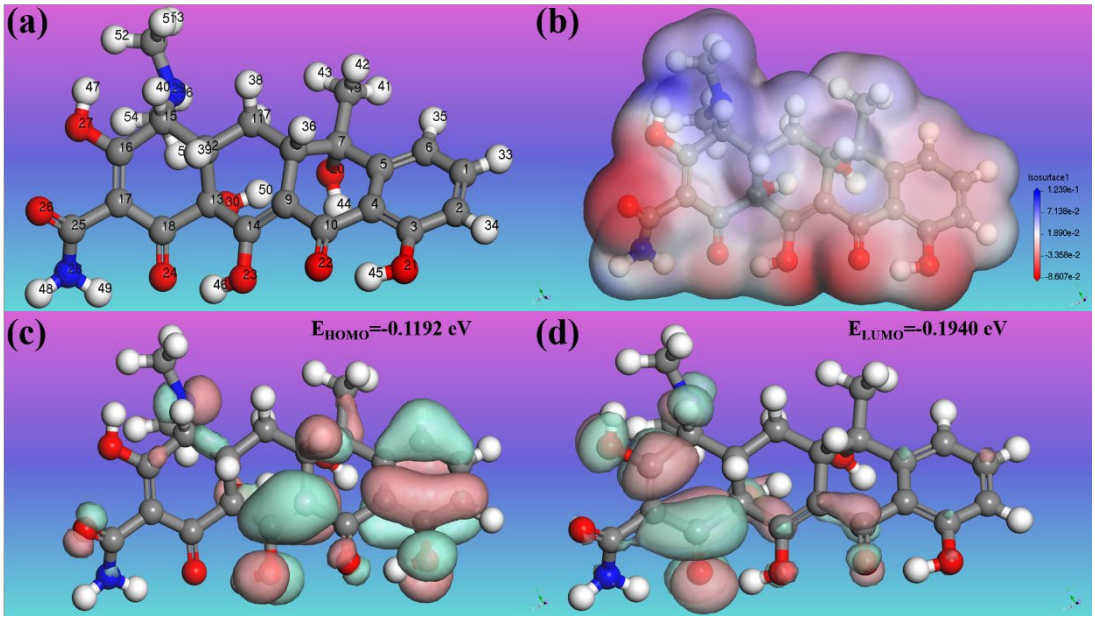

Fig. 8 (a) Chemical structure of TC; (b) electrostatic potential of the TC molecule; (c-d) HOMO and LUMO of TC.

Fig. 8a shows the chemical structure of TC, to further clarify the degradation mechanism of TC, electrostatic potential based on Materials Studio 2019 software with Dmol3 Calculation and GGA/PBE functional were adopted. Obviously, the blue portion of Fig. 8b corresponds to the region with high electron density, while the red portion corresponds to the region with low electron density. The higher the electron density, the more vulnerable to nucleophile attack (such as $\cdot O_2^-$) and the easier the electrophilic substitution reaction. Furthermore, the Fukui function is an essential concept

in the framework of density functional theory. It describes the degree of change in electron density at each position as the system's electron number changes. Table S4 displays the results of the Fukui (-), Fukui (+), Fukui (0) and CDD at different positions in the TC, with larger values indicating more active sites. It can be seen that C (16), C (17), C (18), O (24), O (27) and N (29) are easily attacked by $\cdot O_2^-$[54].To assess the stability of TC molecules, the energy difference between HOMO and LUMO energies ($\Delta E = E_{LUMO} - E_{HOMO}$) was calculated according to Fig. 8c and d, and ΔE = 0.0748 eV was obtained. The lower the value of ΔE, the greater the molecule's activity. The Hirshfeld charge was used to analyze the substituent localization effect of TC in Table S4, and the results were consistent with the experimental results.

The ring structure of TC molecules is obviously linked to a variety of ionizable functional groups and electron-rich groups, such as dimethyl amino group, phenol group, conjugated double bond and so on. A large number of strong oxidants ($\cdot OH$, $\cdot O_2^-$ and H_2O_2) will destroy these groups, resulting in some small molecular organics or organics that are difficult to degrade[55]. Based on the Fukui index, the degradation mechanism was further revealed and the main possible degradation products were inferred. TC electrolyzed for 120 min under ideal conditions were detected by LC-MS, and intermediate mass spectrograms were provided (Fig. S4-S7). Five major degradation pathways are shown below. Normally, we can determine that m/z = 445.16 represents TC since this is consistent with its molecular weight. First, due to dehydration and the formation of ester groups, TC is decomposed into product E (m/z = 410.12)[56]. Simultaneously, the deamidation reaction results in the loss of the amino and carbonyl groups, yielding product D (m/z = 418.17). By dehydroxylation, demethylation, amino group removal and $\cdot OH$ attack, product D forms intermediates H (m/z = 362.32) and G (m/z = 274.27). Additionally, since the double bond at C_9-C_{14} position has a high

electron density and is a relatively active electrophilic site, it will be preferentially attacked by nucleophiles (·OH), resulting in the occurrence of hydroxylation reaction. Eventually, the structure of the TC molecule changes, resulting in the production of an intermediate product A (m/z = 460.27)[57] with a higher molecular weight. Product B (m/z = 418.17) is attributed to deamidation, which can be converted to product C (m/z = 353.25) by removing hydroxyl, methyl and amino groups. Product A undergoes demethylation, deamination and continuous ring-opening reactions to generate product F (m/z = 412.13). The intermediates are further broken down into small organic molecules (products I (m/z = 230.25)[58] and J (m/z = 146.98)) by the ring-opening reaction and the removal of some functional groups. Eventually, as the oxidative degradation process continues, these small molecules are mineralized into carbon dioxide, water and other inorganic ions.

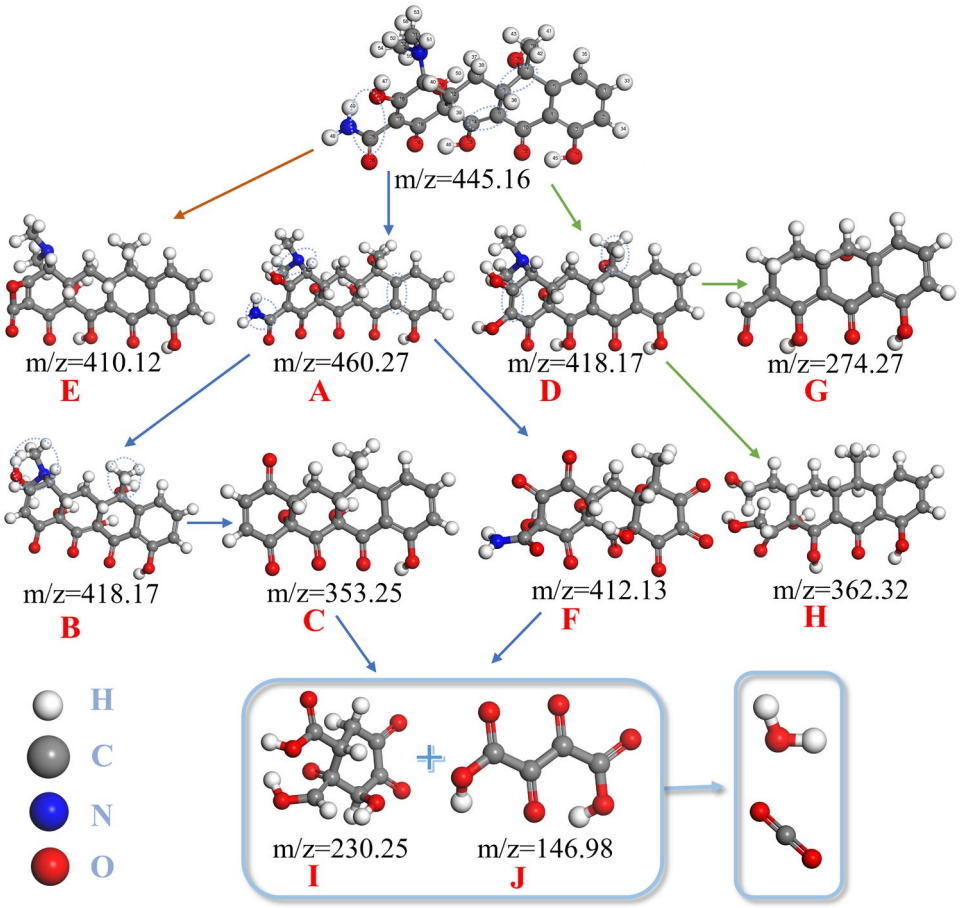

Fig. 9 Possible degradation pathways of TC in the ZrO_2-MnO_x/Nano-G system.

To more thoroughly assess the degradation effect of the ZrO_2-MnO_x/Nano-G composite electrode, it was compared to previously reported results (Table S3). It is clear that these materials degrade well under various treatment methods. However, the ZrO_2-MnO_x/Nano-G electrode requires less reaction time and has a wide range of applications in TC degradation.

4. Conclusions

In summary, transition metal oxide doped graphite nanoelectrodes (ZrO_2-MnO_x/Nano-G) were prepared using the sol-gel and hot-pressing methods. ZrO_2-MnO_x/Nano-G electrodes outperform Nano-G and MnO_x/Nano-G electrodes in terms of active area, charge transfer resistance and electrochemical performance. Then ZrO_2-MnO_x/Nano-G was used to evaluate the electrochemical degradation of TC, and the degradation reaction was in accordance with the quasi-first-order kinetic model. The optimal parameters for electrocatalytic degradation of TC were determined as follows: at pH 5.0, the initial concentration of TC was 20 mg L^{-1}, the current density was 30 mA cm^{-2}, the electrode distance was 10 mm, and the supporting electrolyte was 0.1 mol L^{-1} Na_2SO_4. Under these conditions, the degradation rate of TC can reach 93% after 120 min electrolysis. After 10 cycles of degradation experiments, ZrO_2-MnO_x/Nano-G showed good stability. The identification of small non-toxic intermediates of TC by LC-MS indicated that TC was first degraded to non-toxic small molecules and then decomposed to CO_2 and H_2O. It provides theoretical basis and experimental reference for the electrochemical treatment of antibiotic wastewater.

Author contributions

Si Duan and Xiaoting Yang equally contributed to this work by conducting experiments, validation and data collation. Si Duan completed writing this manuscript, discussed it with Guihong Lan, and Yongqiang Liu and Zhuang Xie provided help with theoretical analysis. Yuan Gao carried out the

theoretical calculations. Zhuang Xie provided assistance in the drawing of mechanism diagrams. All authors discussed the results and commented on the manuscript.

Conflicts of interest

The authors declare that they have no known competing financial interests or personal relationships that could have appeared to influence the work reported in this paper.

Acknowledgements

This work was supported by the project of Chuanqing Drilling Engineering Co., LTD. - Southwest Petroleum University, "In-depth Study on Microbial Corrosion of Weiyuan Shale Gas and Optimization Evaluation of Prevention and Control Measures"(CQXN-2021-10).

Reference

1 C. Bai, G. Yang and S. Zhang, et al., A synergistic system of electrocatalytic-anode/alpha-MnO_2/peroxymonosulfate for removing combined pollution of tetracycline and Cr (VI), *Chem. Eng. J.*, 2021, **423**, 130284.

2 J. Tang, J. Fang and N. Tam, et al., Impact of Phytoplankton Blooms on Concentrations of Antibiotics in Sediment and Snails in a Subtropical River, China, *Environ. Sci. Technol.*, 2021, **55**, 1811–1821.

3 G. Penalva, R. Benavente and M. Perez-Moreno, et al., Effect of the coronavirus disease 2019 pandemic on antibiotic use in primary care, *Clin. Microbiol. Infect.*, 2021, **27**, 1058–1060.

4 V. Santas-Miguel, M. Fernandez-Sanjurjo, A. Nunez-Delgado, et al., Use of biomass ash to reduce toxicity affecting soil bacterial community growth due to tetracycline antibiotics, *J. Environ. Manage.*, 2020, **269**, 110838.

5 W. Yan, Y. Xiao and W. Yan, et al., The effect of bioelectrochemical systems on antibiotics removal and antibiotic resistance genes: A review, *Chem. Eng. J.*, 2019, **358**, 1421–1437.

6 M. Kumar, S. Ambika and A. Hassani, et al., Waste to catalyst: Role of agricultural waste in water and wastewater treatment, *Sci. Total Environ.*, 2023, **858**, 159762.

7 Z. Yang, Q. Lin and G. Zeng, et al., Ternary hetero-structured BiOBr/Bi_2MoO_6@MXene composite membrane: Construction and enhanced removal of antibiotics and dyes from water, *J. Membr. Sci.*, 2023, **669**, 121329.

8 Z. Yang, J. Cao and Y. Chen, et al., Mn-doped zirconium metal-organic framework as an effective adsorbent for removal of tetracycline and Cr (VI) from aqueous solution, *Microporous Mesoporous Mater.*, 2019, **277**, 277–285.

9 Z. Chu, B. Zheng and W. Wang, et al., Magnetic Nitrogen-Doped biochar for adsorptive and oxidative removal of antibiotics in solutions, *Sep. Purif. Technol.*, 2022, **297**, 121508.

10 J. Wang, X. Yi and X. Xu, et al., Eliminating tetracycline antibiotics matrix via photoactivated sulfate radical-based advanced oxidation process over the immobilized MIL-88A: Batch and continuous experiments, *Chem. Eng. J.*, 2022, **431**, 133213.

11 O. Degorska, J. Zdarta and K. Synoradzki, et al., From core-shell like structured zirconia/magnetite hybrid towards novel biocatalytic systems for tetracycline removal: Synthesis, enzyme immobilization, degradation and toxicity study, *J. Environ. Chem. Eng.*, 2021, **9**, 105701.

12 X. Shi, L. Wang and A. Zuh, et al., Photo-Fenton reaction for the degradation of tetracycline hydrochloride using a $FeWO_4$/BiOCl nanocomposite, *J. Alloys Compd.*, 2022, **903**, 163889.

13 C. Wang, C. Lin and G. Liao, Degradation of antibiotic tetracycline by ultrafine-bubble ozonation process, *J. Water Process. Eng.*, 2020, **37**, 101463.

14 M. Wang, Y. Zhang and D. Chen, et al., Biomimetic porphyrin-modified 3D porous composite material adsorption enhances photocatalytic CO_2 reduction and tetracycline oxidative degradation, *Chem. Eng. J.*, 2023, **469**, 144064.

15 S. Yang, Y. Feng and D. Gao, et al., Electrocatalysis degradation of tetracycline in a three-dimensional aeration electrocatalysis reactor (3D-AER) with a flotation-tailings particle electrode (FPE): Physicochemical properties, influencing factors and the degradation mechanism, *J. Hazard. Mater.*, 2021, **407**, 124361.

16 H. Sun, F. He and W. Choi, Production of Reactive Oxygen Species by the Reaction of Periodate and Hydroxylamine for Rapid Removal of Organic Pollutants and Waterborne Bacteria, *Environ. Sci. Technol.*, 2020, **54**, 6427–6437.

17 P. Ashrafi, D. Nematollahi and A. Shabanloo, et al., A detailed electrochemical study of anti-malaria drug hydroxychloroquine: Application of a highly porous 3D multi-metal oxide carbon felt/beta-PbO_2-ZrO_2-MoO_x electrode for its electrocatalytic degradation, *Electrochim. Acta*, 2023, **458**, 142555.

18 X. Mi, M. Yang and L. Xie, et al., RGO/MoS_2/$Ce_{0.75}Zr_{0.25}O_2$ electro-Fenton cathode with higher matching and complementarity for efficient degradation of ciprofloxacin, *Catal. Today*, 2020, **339**, 371–378.

19 K. Araujo, E. dos Santos and M. Pierpaoli, et al., Diamondized carbon nanoarchitectures as electrocatalytic material for sulfate-based oxidizing species electrogeneration, *Electrochim. Acta*, 2022, **430**, 141069.

20 M. Kim, K. Firestein and J. Fernando, et al., Strategic design of Fe and N co-doped hierarchically porous carbon as superior ORR catalyst: from the perspective of nanoarchitectonics, *Chem. Sci.*,

2022, **13**, 10836–10845.

21 R. Gupta, V. Ganesan and P. K. Sonkar, et al., Phenosafranine encapsulated mesoporous silica as efficient electrocatalyst for Cr (VI) reduction and its subsequent sensitive determination, *Microchem. J.*, 2023, **193**, 109193.

22 M. Kim, X. Xu and R. Xin, et al., KOH-Activated Hollow ZIF-8 Derived Porous Carbon: Nanoarchitectured Control for Upgraded Capacitive Deionization and Supercapacitor, *ACS Appl. Mater. Interfaces*, 2021, **13**, 52034–52043.

23 M. Kim, R. Xin and J. Earnshaw, et al., MOF-derived nanoporous carbons with diverse tunable nanoarchitectures, *Nat. Protoc.*, 2022, **17**, 2990-+.

24 Y. Wei, B. Li and X. Wang, et al., Magnified fluorescence detection of silver(I) ion in aqueous solutions by using nano-graphite-DNA hybrid and DNase I, *Biosens. Bioelectron.*, 2014, **58**, 276–281.

25 Z. Song, Y. Ma and C. Li, The residual tetracycline in pharmaceutical wastewater was effectively removed by using MnO_2/graphene nanocomposite, *Sci. Total Environ.*, 2019, **651**, 580–590.

26 Z. Liu, A. Zhang and Y. Liu, et al., Local surface plasmon resonance (LSPR)-coupled charge separation over g-C_3N_4-supported WO_3/BiOCl heterojunction for photocatalytic degradation of antibiotics, *Colloids Surf., A*, 2022, **643**, 128818.

27 B. Tang, J. Du and Q. Feng, et al., Enhanced generation of hydroxyl radicals on well-crystallized molybdenum trioxide/nano-graphite anode with sesame cake-like structure for degradation of bio-refractory antibiotic, *J. Colloid Interface Sci.*, 2018, **517**, 28–39.

28 D. Li, X. Guo and H. Song, et al., Preparation of RuO_2-TiO_2/Nano-graphite composite anode for electrochemical degradation of ceftriaxone sodium, *J. Hazard. Mater.*, 2018, **351**, 250–259.

29 Zhengyi Li, Peng Zhou and Min Zhou, et al., Synergistic electrocatalysis of crystal facet and O-vacancy for enhancive urea synthesis from nitrate and CO_2, *Appl. Catal., B*, 2023, **338**, 122962.

30 A. Zhang, Y. Liang and H. Zhang, et al., Doping regulation in transition metal compounds for electrocatalysis, *Chem. Soc. Rev.*, 2021, **50**, 9817–9844.

31 K. Ding, X. Zhang and F. Xia, et al., Surface charge transfer doping induced inversion layer for high-performance graphene/silicon heterojunction solar cells, *J. Mater. Chem. A*, 2017, **5**, 285–291.

32 Y. Sa, S. Kim and Y. Lee, et al., Mesoporous Manganese Oxides with High-Valent Mn Species and Disordered Local Structures for Efficient Oxygen Electrocatalysis, *ACS Appl. Mater. Interfaces*, 2023, **15**, 31393–31402.

33 W. Wang, J. Yu and J. Zou, et al., Mechanism for enhancing biodegradability of antibiotic pharmacy wastewater by in-situ generation of H_2O_2 and radicals over MnO_x/nano-G/2-EAQ/AC cathode, *Electrochim. Acta*, 2016, **191**, 426–434.

34 A. Chauhan, N. Dhenadhayalan and J. Yeh, et al., Photocatalytic degradation-based efficient elimination of pesticides using ruthenium/gold metal nanoparticle-anchored zirconium dioxide, *New J. Chem.*, 2022, **46**, 22561–22573.

35 O. Ama, N. Mabuba and O. Arotiba, Synthesis, Characterization, and Application of Exfoliated Graphite/Zirconium Nanocomposite Electrode for the Photoelectrochemical Degradation of Organic Dye in Water, *Electrocatalysis*, 2015, **6**, 390–397.

36 X. Yu, T. Sun and J. Wan, Preparation for Mn/Nanographite Materials and Study on Electrochemical Degradation of Phenol by Mn/Nanographite Cathodes, *J. Nanosci. Nanotechnol.*, 2014, **14**, 6835–6840.

37 B. Tang, J. Du and Q. Feng, et al., Enhanced generation of hydroxyl radicals on well-crystallized molybdenum trioxide/nano-graphite anode with sesame cake-like structure for degradation of bio-refractory antibiotic, *J. Colloid Interface Sci.*, 2018, **517**, 28–39.

38 F. Khodabandeloo, M. Sheydaei and P. Moharramkhani, et al., Preparation of $Fe_2(MoO_4)_3$/graphene/Ti nanocomposite electrode for visible-light photoelectrocatalytic degradation of organic pollutants, *Chemosphere*, 2023, **330**, 138766.

39 O. Ama, K. Khoele and W. Anku, et al., Synthesis and Application of MnO_2/Exfoliated Graphite Electrodes for Enhanced Photoelectrochemical Degradation of Methylene Blue and Congo Red Dyes in Water, *Electrocatalysis*, 2020, **11**, 413–421.

40 O. Ama, A. Wilson and S. Ray, Photoelectrochemical degradation of methylene blue dye under visible light irradiation using EG/Ag-ZrO_2 nanocomposite electrodes, *Int. J. Electrochem. Sci.*, 2019, **14**, 9982–10001.

41 Y. Zhu, Y. Pan and Y. Zhu, et al., Efficient electrocatalytic formic acid oxidation over PdAu-manganese oxide/carbon, *J. Colloid Interface Sci.*, 2021, **593**, 244–250.

42 P. Ding, H. Ji and P. Li, et al., Visible-light degradation of antibiotics catalyzed by titania/zirconia/graphitic carbon nitride ternary nanocomposites: a combined experimental and theoretical study, *Appl. Catal., B*, 2022, **300**, 118699.

43 J. Tian, Q. Shao and J. Zhao, et al., Microwave solvothermal carboxymethyl chitosan templated synthesis of TiO_2/ZrO_2 composites toward enhanced photocatalytic degradation of Rhodamine B, *J. Colloid Interface Sci.*, 2019, **541**, 18–29.

44 Xue Xin, Qiming Qu and Islam E. Khalil, et al., Hetero-phase zirconia encapsulated with Au nanoparticles for boosting electrocatalytic nitrogen reduction, *Chin. Chem. Lett.*, ,

DOI:10.1016/j.cclet.2023.108654.

45 T. Gopi, G. Swetha and S. Shekar, et al., Catalytic decomposition of ozone on nanostructured potassium and proton containing delta-MnO_2 catalysts, *Catal. Commun.*, 2017, **92**, 51–55.

46 L. Mao, Z. Chen and X. Wu, et al., Plasma-catalyst hybrid reactor with CeO_2/gamma-Al_2O_3 for benzene decomposition with synergetic effect and nano particle by-product reduction, *J. Hazard. Mater.*, 2018, **347**, 150–159.

47 Y. Xiao and M. Cao, Carbon-Anchored MnO Nanosheets as an Anode for High-Rate and Long-Life Lithium-Ion Batteries, *ACS Appl. Mater. Interfaces*, 2015, **7**, 12840–12849.

48 P. Duan, S. Gao and X. Li, et al., Preparation of CeO_2-ZrO_2 and titanium dioxide coated carbon nanotube electrode for electrochemical degradation of ceftazidime from aqueous solution, *J. Electroanal. Chem.*, 2019, **841**, 10–20.

49 C. Shi, S. Yu and C. Li, Fabrication of aligned carbon nanofiber doped with SnO_2-Sb for efficient electrochemical removal of tetracycline, *Chem. Eng. J.*, 2022, **441**, 136052.

50 Y. Wang, C. Shen and M. Zhang, et al., The electrochemical degradation of ciprofloxacin using a SnO_2-Sb/Ti anode: Influencing factors, reaction pathways and energy demand, *Chem. Eng. J.*, 2016, **296**, 79–89.

51 F. Meng, Y. Wang and Z. Chen, et al., Synthesis of CQDs@FeOOH nanoneedles with abundant active edges for efficient electro-catalytic degradation of levofloxacin: Degradation mechanism and toxicity assessment, *Appl. Catal., B*, 2021, **282**, 119597.

52 X. Li, C. Xiao and X. Ruan, et al., Enrofloxacin degradation in a heterogeneous electro-Fenton system using a tri-metal-carbon nanofibers composite cathode, *Chem. Eng. J.*, 2022, **427**, 130927.

53 J. Wang, D. Zhi and H. Zhou, et al., Evaluating tetracycline degradation pathway and

intermediate toxicity during the electrochemical oxidation over a Ti/Ti_4O_7 anode, *Water Res.*, 2018, **137**, 324–334.

54 B. Ma, S. Xin and Y. Xin, et al., Visible-light-driven photoelectrocatalytic degradation of p-chloronitrobenzene by BiOBr/TiO_2 nanotube arrays photoelectrodes: Mechanisms, degradation pathway and DFT calculation, *Sep. Purif. Technol.*, 2021, **268**, 118699.

55 F. Yu, S. Wang and H. Ma, Co-catalysis of metal sulfides accelerating Fe^{2+}/Fe^{3+} cycling for the removal of tetracycline in heterogeneous electro-Fenton using a novel rolled NPC/CB cathodes, *Sep. Purif. Technol.*, 2021, **275**, 119200.

56 S. Chen, L. Tang and H. Feng, et al., Carbon felt cathodes for electro-Fenton process to remove tetracycline via synergistic adsorption and degradation, *Sci. Total Environ.*, 2019, **670**, 921–931.

57 Y. Chen and K. Liu, Preparation and characterization of nitrogen-doped TiO_2/diatomite integrated photocatalytic pellet for the adsorption-degradation of tetracycline hydrochloride using visible light, *Chem. Eng. J.*, 2016, **302**, 682–696.

58 S. Yang, Y. Feng and D. Gao, et al., Electrocatalysis degradation of tetracycline in a three-dimensional aeration electrocatalysis reactor (3D-AER) with a flotation-tailings particle electrode (FPE): Physicochemical properties, influencing factors and the degradation mechanism, *J. Hazard. Mater.*, 2021, **407**, 124361.